

# Self-induced optical modulation of the transmission through a high- $Q$ silicon microdisk resonator

Thomas J. Johnson, Matthew Borselli and Oskar Painter

Thomas J. Watson, Sr., Laboratory of Applied Physics, California Institute of Technology,  
Pasadena, CA 91125 USA

phone: (626) 395-6160, fax: (626) 795-7258

[tjrj@caltech.edu](mailto:tjrj@caltech.edu)

**Abstract:** Direct time-domain observations are reported of a low-power, self-induced modulation of the transmitted optical power through a high- $Q$  silicon microdisk resonator. Above a threshold input power of 60  $\mu\text{W}$  the transmission versus wavelength deviates from a simple optical bistability behavior, and the transmission intensity becomes highly oscillatory in nature. The transmission oscillations are seen to consist of a train of sharp transmission dips of width approximately 100 ns and period close to 1  $\mu\text{s}$ . A model of the system is developed incorporating thermal and free-carrier dynamics, and is compared to the observed behavior. Good agreement is found, and the self-induced optical modulation is attributed to a nonlinear interaction between competing free-carrier and phonon populations within the microdisk.

© 2006 Optical Society of America

**OCIS codes:** (230.5750) Resonators; (190.4870) Optically induced thermo-optical effects

---

## References and links

1. R. A. Soref and J. P. Lorenzo, "All-Silicon Active and Passive Guided-Wave Components for  $\lambda = 1.3$  and  $1.6\mu\text{m}$ ," *IEEE J. Quantum Electron.* **22**, 873–879 (1986).
2. P. E. Barclay, K. Srinivasan, and O. Painter, "Nonlinear response of silicon photonic crystal microresonators excited via an integrated waveguide and a fiber taper," *Opt. Express* **13**, 801–820 (2005), <http://www.opticsexpress.org/abstract.cfm?URI=OPEX-13-3-801>.
3. M. Notomi, A. Shinya, S. Mitsugi, G. Kira, E. Kuramochi, and T. Tanabe, "Optical bistable switching action of Si high- $Q$  photonic-crystal nanocavities," *Opt. Express* **13**, 2678–2687 (2005), <http://www.opticsexpress.org/abstract.cfm?URI=OPEX-13-7-2678>.
4. T. Tanabe, M. Notomi, S. Mitsugi, A. Shinya, and E. Kuramochi, "All-optical switches on a silicon chip realized using photonic-crystal nanocavities," *Appl. Phys. Lett.* **87**, 151112–1–151112–3 (2005).
5. S. F. Preble, Q. Xu, B. S. Schmidt, and M. Lipson, "Ultrafast all-optical modulation on a silicon chip," *Opt. Lett.* **30**, 2891–2893 (2005).
6. T. Tanabe, M. Notomi, S. Mitsugi, A. Shinya, and E. Kuramochi, "Fast bistable all-optical switch and memory on a silicon photonic crystal on-chip," *Opt. Lett.* **30**, 2575–2577 (2005).
7. M. Borselli, T. J. Johnson, and O. Painter, "Nonlinear Optics in High- $Q$  SOI Optical Microcavities," In *Integrated Photonics Research and Applications/Nanophotonics for Information Systems Topical Meetings on CD-ROM*, (OSA, Washington, DC, 2005).
8. T. J. Johnson, M. Borselli, and O. Painter, "Self-generated optical modulation in a high- $Q$  SOI microdisk resonator," In *Frontiers in Optics 2005/Laser Science XXI*, (OSA, Washington, DC, 2005).
9. G. Priem, P. Dumon, W. Bogaerts, D. V. Thourhout, G. Morthier, and R. Baets, "Optical bistability and pulsating behaviour in Silicon-On-Insulator ring resonator structures," *Opt. Express* **13**, 9623–9628 (2005), <http://www.opticsexpress.org/abstract.cfm?URI=OPEX-13-23-9623>.
10. S. L. McCall, "Instability and regenerative pulsation phenomena in Fabry-Perot nonlinear optic media devices," *Appl. Phys. Lett.* **32**, 284–286 (1978).

11. H. M. Gibbs, J. L. Jewell, J. V. Moloney, K. Tai, S. Tarng, D. A. Weinberger, A. C. Gossard, S. L. McCall, A. Passner, and W. Weigmann, "Optical Bistability, Regenerative Pulsations, and Transverse Effects in Room-Temperature GaAs-AlGaAs Superlattice etalons," *J. Phys. (Paris)* **44**, 195–204 (1983).
12. J. L. Jewell, H. M. Gibbs, S. S. Tarng, A. C. Gossard, and W. Weigmann, "Regenerative pulsations from an intrinsic bistable device," *Appl. Phys. Lett.* **40**, 291–293 (1982).
13. R. K. Jain and D. G. Steel, "Degenerate four-wave mixing of 10.6  $\mu\text{m}$  radiation in  $\text{Hg}_{1-x}\text{Cd}_x\text{Te}$ ," *Appl. Phys. Lett.* **37**, 1–3 (1980).
14. A. E. Fomin, M. L. Gorodetsky, I. S. Grudin, and V. S. Ilchenko, "Nonstationary nonlinear effects in optical microspheres," *J. Opt. Soc. Am. B* **22**, 459–465 (2005).
15. M. Borselli, T. J. Johnson, and O. Painter, "Beyond the Rayleigh scattering limit in high-Q silicon microdisks: theory and experiment," *Opt. Express* **13**, 1515–1530 (2005), <http://www.opticsexpress.org/abstract.cfm?URI=OPEX-13-5-1515>.
16. K. Srinivasan, P. E. Barclay, M. Borselli, and O. Painter, "Optical-fiber-based measurement of an ultrasmall volume, high-Q photonic crystal microcavity," *Phys. Rev. B* **70**, 081306(R) (2004).
17. M. Borselli, K. Srinivasan, P. E. Barclay, and O. Painter, "Rayleigh scattering, mode coupling, and optical loss in silicon microdisks," *Appl. Phys. Lett.* **85**, 3693–3695 (2004).
18. M. Gorodetsky and V. Ilchenko, "Thermal Nonlinear Effects in Optical Whispering Gallery Microresonators," *Laser Phys.* **2**, 1004–1009 (1992).
19. D. Weiss, V. Sandoghdar, J. Hare, V. Lefèvre-Seguin, J. Raimond, and S. Haroche, "Splitting of high-Q Mie modes induced light backscattering in silica microspheres," *Opt. Lett.* **22**, 1835–1837 (1995).
20. T. J. Kippenberg, S. M. Spillane, and K. J. Vahala, "Modal coupling in traveling-wave resonators," *Opt. Lett.* **27**, 1669–1671 (2002).
21. M. Gorodetsky, A. Pryamikov, and V. Ilchenko, "Rayleigh scattering in high-Q microspheres," *J. Opt. Soc. Am. B* **17**, 1051–1057 (2000).
22. T. Carmon, L. Yang, and K. J. Vahala, "Dynamical thermal behavior and thermal self-stability of microcavities," *Opt. Express* **12**, 4742–4750 (2004), <http://www.opticsexpress.org/abstract.cfm?URI=OPEX-12-20-4742>.
23. V. R. Almeida and M. Lipson, "Optical bistability on a silicon chip," *Opt. Lett.* **29**, 2387–2389 (2004).
24. H. M. Gibbs, *Optical Bistability: Controlling Light with Light* (Academic Press, San Diego, CA, 1985).
25. G. Cocorullo and I. Rendina, "Thermo-optical modulation at 1.5  $\mu\text{m}$  in silicon etalon," *Electron. Lett.* **28**, 83–85 (1992).
26. K. J. Vahala, "Optical Microcavities," *Nature (London)* **424**, 839–846 (2003).
27. Here we assume that the coupling to each of the standing-wave modes is identical. In general, the coupling can be different, although experimentally we have noticed only small differences in coupling.
28. R. Claps, V. Raghunathan, D. Dimitropoulos, and B. Jalali, "Influence of nonlinear absorption on Raman amplification in silicon waveguides," *Opt. Express* **12**, 2774–2780 (2004), <http://www.opticsexpress.org/abstract.cfm?URI=OPEX-12-12-2774>.
29. Note that the confinement factor and effective mode volume for the two standing-wave modes are identical, hence we drop the  $c/s$  subscript.
30. For TPA with the standing wave modes one has an additional term dependent upon the product  $U_c U_s$ , with cross-confinement factor  $\Gamma_{c/s, \text{TPA}}$  and cross-mode volume  $3V_{c/s, \text{TPA}}$  pre-factors. For FCA, described below, one cannot write the total absorption just in terms of products of powers of the cavity energies, but rather the mode amplitudes themselves must be explicitly used.
31. R. A. Soref and B. R. Bennett, "Electrooptical Effects in Silicon," *IEEE J. Quantum Electron.* **23**, 123–129 (1987).
32. S. G. Johnson, M. Ibanescu, M. A. Skorobogatiy, O. Weisberg, J. D. Joannopoulos, and Y. Fink, "Perturbation theory for Maxwell's equations with shifting material boundaries," *Phys. Rev. E* **65**, 066611 (2002).
33. A variable order Adams-Bashforth-Moulton predictor-corrector method was used.
34. *Handbook of optical constants of solids*, E. Palick, ed., (Academic Press, Boston, MA, 1985).
35. M. Dinu, F. Quochi, and H. Garcia, "Third-order nonlinearities in silicon at telecom wavelengths," *Appl. Phys. Lett.* **82**, 2954–2956 (2003).
36. D. K. Schroder, R. N. Thomas, and J. C. Swartz, "Free Carrier Absorption in Silicon," *IEEE Trans. Electron. Dev.* **25**, 254–261 (1978).
37. S. Sze, *Physics of Semiconductor Devices*, 2nd ed. (John Wiley and Sons, New York, New York, 1981).
38. S. Wiggins, *Introduction to Applied Nonlinear Dynamical Systems and Chaos*, 2nd ed. (Springer-Verlag New York, New York, NY, 2003).
39. K. Aubin, M. Zalalutdinov, T. Alan, R. Reichenbach, R. Rand, A. Zehnder, J. Parpia, and H. Craighead, "Limit Cycle Oscillations in CW Laser Driven NEMS," *J. Microelectromech. Syst.* **13**, 1018–1026 (2004).
40. Q. Xu, B. Schmidt, S. Pradhan, and M. Lipson, "Micrometre-scale silicon electro-optic modulator," *Nature* **435**, 325–327 (2005).
41. Luxtera, [http://www.luxtera.com/news\\_press.htm#081505](http://www.luxtera.com/news_press.htm#081505).
42. V. R. Almeida, C. A. Barrios, R. R. Panepucci, and M. Lipson, "All-optical control of light on a silicon chip," *Nature* **431**, 1081–1084 (2004).

43. A. Liu, R. Jones, L. Liao, D. Samara-Rubio, D. Rubin, O. Cohen, R. Nicolaescu, and M. Paniccia, "A high-speed silicon optical modulator based on a metal-oxide-semiconductor capacitor," *Nature* **427**, 615–618 (2004).
  44. H. Rong, R. Jones, A. Liu, O. Cohen, D. Hak, A. Fang, and M. Paniccia, "A continuous-wave Raman silicon laser," *Nature* **433**, 725–728 (2005).
  45. B.-S. Song, S. Noda, T. Asano, and Y. Akahane, "Ultra-high- $Q$  photonic double-heterostructure nanocavity," *Nature Materials* **4**, 207–210 (2005).
- 

## 1. Introduction

Despite the current lack of an efficient electrically pumped light emitter in the silicon material system, the infrastructure and knowledge built up by the microelectronics industry has long rendered it attractive to many in the optoelectronics field [1]. Silicon is a high index of refraction material ( $n = 3.48$  at  $\lambda = 1.5 \mu\text{m}$ ), and because  $\text{SiO}_2$  and  $\text{SiN}_x$  have relatively low index ( $n = 1.4 - 2.0$  at  $\lambda = 1.5 \mu\text{m}$ ), high index-contrast optical structures can be fabricated in the silicon material system in a manner compatible with conventional microelectronics processing. This is important both because one of the chief engines of performance improvement in the microelectronics industry has been the scaling and dense integration of devices, and because the integration of microphotonic devices with microelectronic devices will add functionality to both. In order to achieve scaling with microphotonic devices, high index-contrast devices will be necessary. The scaling of microphotonic devices can also improve their performance by reducing input powers required for certain functionalities [2, 3, 4, 5], or even by making novel functionalities possible [6]. However, as with microelectronics, where scaling devices can lead to unintentional interactions between devices and phenomena, scaling microphotonic devices can also promote unwanted, and in some cases, unanticipated effects.

This paper concerns such an unanticipated effect observed in a high- $Q$  silicon-on-insulator (SOI) microdisk optical resonator, first reported in silicon microphotonic resonators in Refs. [7, 8]. More recently, other indirect measurements suggestive of this phenomenon in Si microphotonic devices have been presented as well [9]. The effect observed and discussed is similar to that observed in hybrid and intrinsic systems, presented in Refs. [10, 11, 12, 13], where fast electronic nonlinearities competed with slower thermal nonlinearities in optically resonant devices in other materials systems, resulting in optical transmission pulsations. A similar self-pulsing behavior caused solely by thermo-optical nonlinearity in fused silica microspheres has also been observed and analyzed [14].

In the work presented here, a low power, continuous-wave, laser is evanescently coupled into the whispering gallery modes (WGMs) of a silicon microdisk optical resonator, and the transmitted optical power monitored; radio frequency (RF) oscillations in the transmission are observed. The microdisk optical resonator considered in this work consists of a silicon disk  $4.5 \mu\text{m}$  in radius and  $340 \text{ nm}$  in thickness resting upon an approximately hourglass-shaped  $\text{SiO}_2$  pedestal  $1.2 \mu\text{m}$  high with effective radius  $1.6 \mu\text{m}$ . The silicon is  $p$ -doped with resistivity  $1 - 3 \Omega\text{-cm}$ . The fabrication details of the silicon microdisk considered here can be found in another work [15]. Images of a Si microdisk with fiber-taper coupling are shown in Fig. 1.

An outline of this paper is as follows. In section 2 the method used to characterize the microdisk resonator is described, and low-power measurements of the resonator's response are presented, including time-domain measurements of the self-oscillation phenomenon. A model of the system is presented in section 3, taking into account the various physical effects important in the high- $Q$  SOI microdisk resonator. In section 4 the results of measurement are compared to the model. Finally, a summary and discussion of the results are given in section 5.

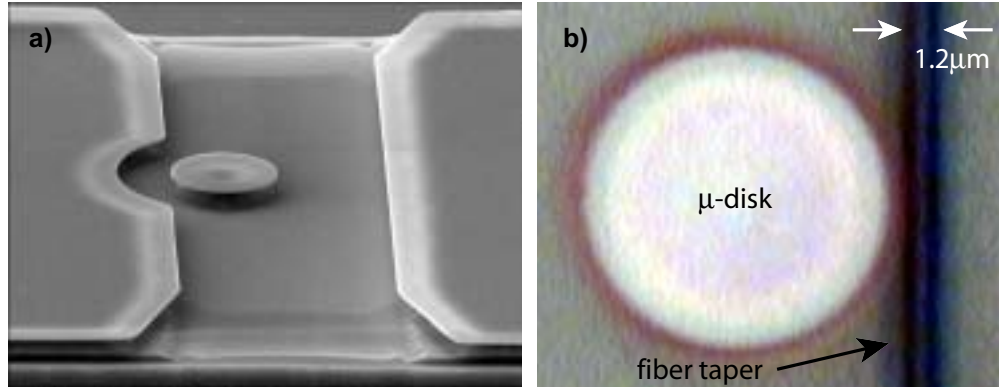


Fig. 1. (a) Scanning electron microscope image of Si microdisk under study. (b) Optical image (top-view) of microdisk with side-coupled optical fiber taper waveguide.

## 2. Measurements

A fiber-taper probe technique is used to excite the WGM resonance [16]. In this technique, a section of a standard single mode fiber is heated in the flame of a hydrogen torch and drawn down to a diameter of  $1.2 \pm 0.2 \mu\text{m}$ . At this diameter, the evanescent field of light guided by the fiber-taper extends significantly into the surrounding air. Using mechanical stages with 50 nm step-size, the tapered fiber can be placed in the near field of the microdisk resonator, where the evanescent field of the light carried by the fiber-taper can be coupled into the WGMs of the microdisk (see Fig. 1(b)). A swept-wavelength tunable laser source is used to measure the transmission spectra of the microdisk resonator WGMs and a manual polarization controller employed to optimize coupling from fiber-taper to WGM. A variable optical attenuator is used to control the amount of power coupled into the fiber-taper. For the high-speed data acquisition measurements of the transmitted optical power described below a New Focus 1554-B 12 GHz photoreceiver was used, either in conjunction with a 22 GHz HP-8563A electronic spectrum analyzer (ESA) for RF power spectrum measurements or an Agilent Infinium 54855A 6 GHz oscilloscope for time-domain measurements.

### 2.1. Low power measurements

At an extremely low input power (all quoted input powers refer to the estimated power at the taper-microdisk junction, where a taper insertion loss of approximately 50% is accounted for) of  $0.5 \mu\text{W}$  we observe (Fig. 2(a)) that the transmission through the coupled microdisk-fiber system displays the characteristic “doublet” lineshape seen in high- $Q$  silicon microdisk resonators [17, 15], and see that the coupling efficiency is approximately 80% at these low input powers. The origin of this feature, described in more detail below, is due to surface-scattering coupling of the clockwise (CW) and counterclockwise (CCW) traveling-wave WGMs of the microdisk resulting in a frequency splitting and formation of standing-wave modes [18, 19, 20, 21]. At these low powers, in absence of nonlinear effects, the intrinsic properties of the doublet modes

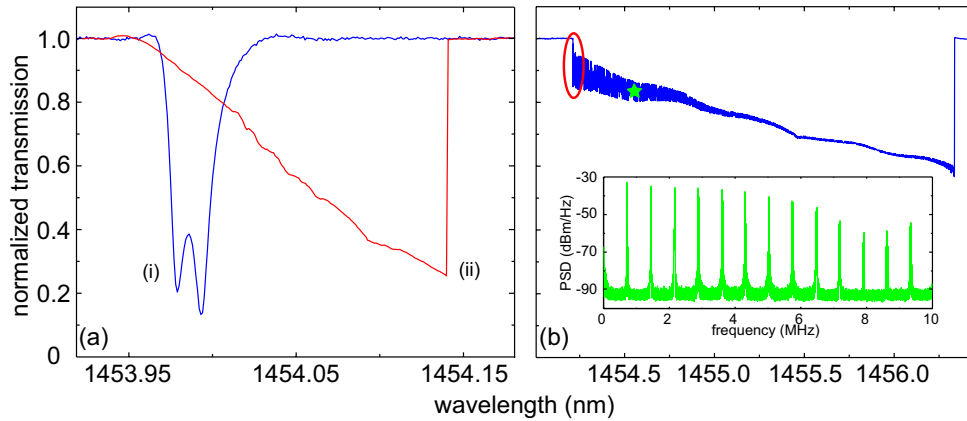


Fig. 2. (a) Normalized optical transmission spectrum of a silicon microdisk WGM resonance at  $0.5\mu\text{W}$  input power (i) and  $35\mu\text{W}$  input power (ii). (b) Normalized transmission with  $480\mu\text{W}$  input power. (inset) Power spectrum of transmission at input wavelength  $\lambda_l = 1454.56\text{nm}$ , indicated by a green star in (b).

can be determined. A fit to the doublet lineshape of Fig. 2(a) yields an intrinsic  $Q$ -factor of  $3.5 \times 10^5$  a CW and CCW traveling-wave mode coupling rate of  $\gamma_\beta = 14.3\text{GHz}$ .

At a slightly higher input power of  $35\mu\text{W}$  we observe (Fig. 2(a) (ii)) a distorted asymmetric lineshape with sharp recovery, characteristic of thermal bistability [2, 22, 23, 24]. In this effect, power absorbed in the microdisk resonator heats the silicon microdisk, causing a red-shift of the resonance wavelength through the thermo-optic effect [25]. If the input laser wavelength is swept from blue to red, the resonance wavelength will be “pushed” ahead of the laser wavelength, resulting in the distorted shape observed in Fig. 2(a) (ii). The sharp recovery occurs when the dropped optical power and thermally induced red-shift reaches its maximum attainable value at resonance. At that point, the input laser cannot further heat the resonator, and the temperature and resonance wavelength quickly return to their initial values, resulting in the sudden increase in transmission. A reversed scan (input laser tuned from red to blue) would result in a qualitatively different transmission spectrum; the system exhibits a hysteresis behavior which, along with the asymmetric transmission spectrum, is characteristic of optical bistability. In the case of a typical resonator, this effect increases with increasing input power. However, in the presence of other phenomena the power-dependent behavior can be significantly altered as described below.

## 2.2. Higher power measurements- time domain behavior

Figure 2(b) shows the transmission spectrum of the resonance depicted in Fig. 2(a) at an input power of  $480\mu\text{W}$ . Note the qualitative differences between Fig. 2(b) and Fig. 2(a): the sudden drop in transmission near  $\lambda_l = 1454\text{nm}$  (red oval), and the fluctuating transmission for laser wavelengths from  $\lambda_l = 1454.3\text{--}1456.2\text{nm}$ . The inset to Fig. 2(b) shows the RF power spectrum of the optical transmission intensity at a laser wavelength in the fluctuating region. Note that the initially continuous-wave input has acquired significant non-zero frequency content with fundamental frequency in the MHz range. The fluctuations in the transmission are thus indicative of a rich time-domain behavior, and are present in the transmission spectrum of this resonance for input powers as low as  $60\mu\text{W}$ .

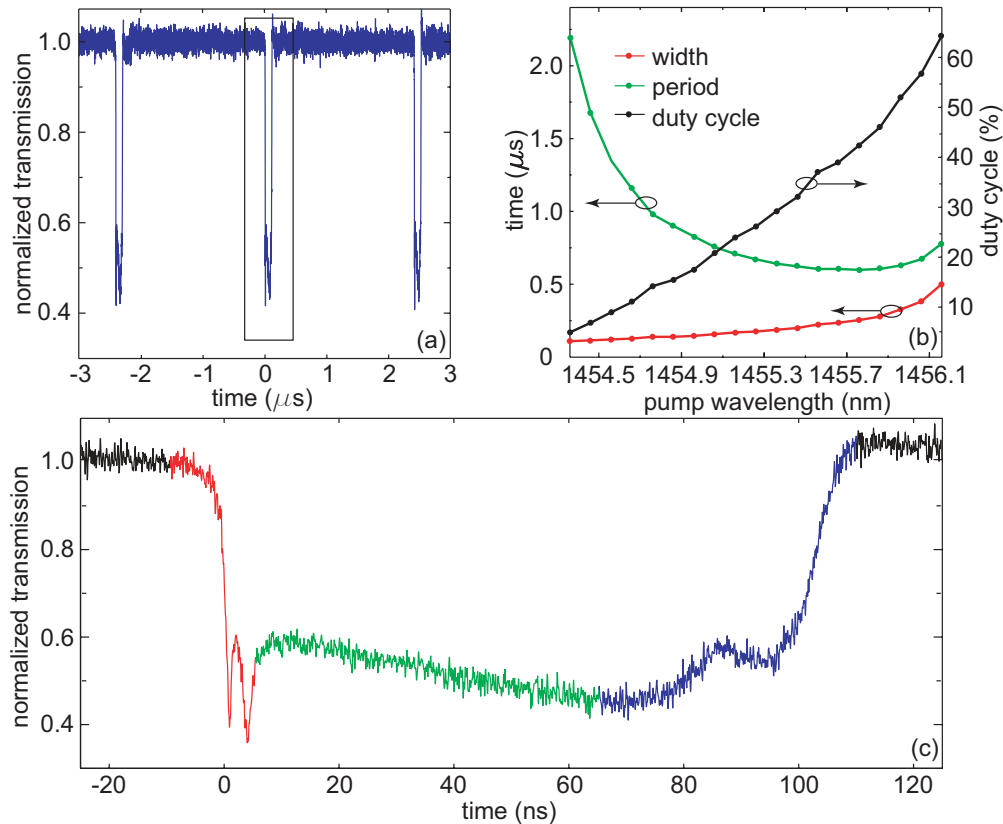


Fig. 3. (a) Time-domain behavior of the transmitted optical power. (b) Dependence of the time-domain behavior upon input laser wavelength. (c) Detail of the transmission oscillation (boxed region in (a)).

Under high speed acquisition, the time-domain behavior of the transmitted optical power is revealed to consist of a periodic train of temporally narrow transmission dips. Figure 3(a) shows a characteristic example of the time-domain behavior. The oscillation begins at the sharp transmission drop near  $\lambda_l = 1454.3$  nm in Fig. 2(b), and persists over the region of fluctuating transmission from  $\lambda_l = 1454.3$ -1456.2 nm. Over this laser tuning range, the period of the oscillation initially decreases and then increases near the end of the oscillation range, while the temporal width of the transmission dip increases monotonically with the laser wavelength. Figure 3(b) depicts the tuning behavior of the period, width, and duty cycle of the oscillations in the transmitted optical power.

Closer study of the temporally narrow transmission dip, depicted in more detail in Fig. 3(c), reveals that near the beginning of the transmission dip (red curve) a fast ( $\sim 2$  ns) double-dip occurs. This is followed by a slow ( $\sim 100$  ns) increase in the transmission depth (green curve). Finally, at the end of the transmission dip (blue curve), just before the transmission recovers, there occurs a more elongated double-dip ( $\sim 20$  ns). In the next section a model is developed to explain these observations in terms of oscillations in the resonance frequencies of the standing-wave WGMs of the Si microdisk due to the nonlinear interaction and competition between free-carriers and phonons generated by optical power circulating within the microdisk.

### 3. Model

The high- $Q$  and small volume of the Si microdisks results in large circulating optical intensities for modest input powers. The circulating intensity,  $I$ , can be approximated by  $I = P \left( \frac{\lambda}{2\pi n_g} \right) \left( \frac{Q}{V} \right)$ , where  $P$  is the input power at wavelength  $\lambda$ ,  $n_g$  is the group index of the resonant mode and  $V$  is the corresponding mode-volume [26]. For the Si microdisk resonators in this work, with  $Q$ -factors of approximately  $3 \times 10^5$  and effective mode volumes of roughly  $40 (\lambda/n_{\text{Si}})^3$ , an input power of 1 mW corresponds to circulating intensities approaching  $500 \text{ MW/cm}^2$ . Such large circulating intensities can result in significant two-photon absorption (TPA) producing heat, free-carriers, and other nonlinearities. The generated free-carriers produce dispersion (FCD), and are themselves optically absorbing (FCA) which produces more heat. The refractive index seen by the circulating light within the microdisk is modified both by the stored thermal energy (phonons) within the microdisk through the thermo-optic effect, and by the dispersion due to the excess of free-carriers. These two effects produce competing shifts in the resonance wavelength of WGMs of the microdisk, red for the thermo-optic shift and blue for the free-carrier dispersion. The shift in the resonance wavelength and the nonlinear absorption in turn alters the circulating optical intensity, which then feeds back and modifies the generation rate of heat and free-carriers. Figure 4 depicts the various physical processes involved in the nonlinear modeling of the Si microdisk. In what follows we incorporate these different processes into an approximate dynamical model for the stored optical energy, free-carriers, and microdisk temperature. We begin with a description of the relevant resonant modes of the Si microdisk.

#### 3.1. Standing wave whispering-gallery-modes

The very low power measurement of the transmission spectrum of the microdisk resonance (illustrated in Fig. 2(a)), displays a characteristic “doublet” lineshape. This can be understood with simple perturbation theory. The ideal circular resonator is azimuthally symmetric, and therefore admits degenerate eigenmodes; it supports a CW propagating mode and a CCW propagating mode with the same frequency. Small departures from perfect circularity and homogeneity of the microdisk, due to imperfections in the fabrication or density variations in the surface material, for example, couple these modes. As a result, the eigenmodes of the perturbed system are cosine- and sine-like standing waves with slightly split frequencies [18, 19]. The equations of motion for the cosine- and sine-like standing wave mode field amplitudes ( $a_c$  and  $a_s$ ) are [20, 21, 15]

$$\frac{da_c}{dt} = \left( -\frac{\gamma_c}{2} + i \left( \Delta\omega_0 + \frac{\gamma_\beta}{2} \right) \right) a_c + \kappa s \quad (1a)$$

$$\frac{da_s}{dt} = \left( -\frac{\gamma_s}{2} + i \left( \Delta\omega_0 - \frac{\gamma_\beta}{2} \right) \right) a_s + \kappa s, \quad (1b)$$

where  $\gamma_c$  ( $\gamma_s$ ) is a phenomenological loss rate for the cosine-like (sine-like) standing wave mode,  $\gamma_\beta$  is the rate of coupling between the ideal CW and CCW traveling wave modes.  $\kappa$  is the coefficient of coupling from the fiber-taper [27],  $\Delta\omega_0$  the detuning of the input light frequency from the center frequency of the doublets, and  $|s|^2$  the input power carried by the fiber-taper. The mode field amplitudes are normalized such that the energies stored in the sine- and cosine-like modes ( $U_s$  and  $U_c$ , respectively) are given by

$$U_s = |a_s|^2 \quad (2a)$$

$$U_c = |a_c|^2. \quad (2b)$$

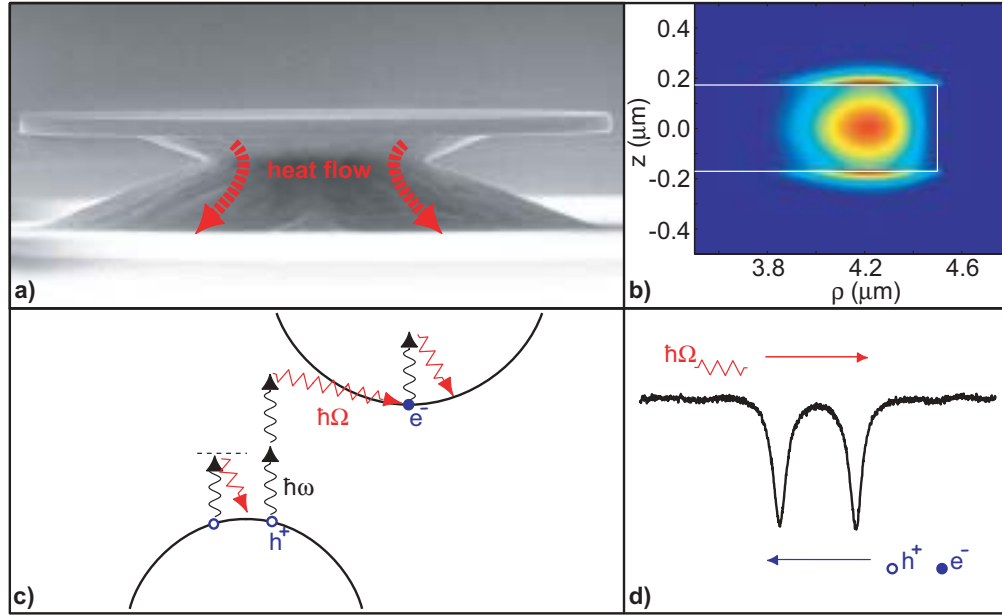


Fig. 4. Picture of the various physical processes involved in the nonlinear model of the Si microdisk considered here. (a) A scanning electron micrograph of a representative SOI microdisk resonator. As discussed below, heat flows by conduction through the SiO<sub>2</sub> pedestal. (b) Square-magnitude of the electric field for the WGM under consideration as calculated by finite-element method. High intensity fields are found in the red regions. High field strengths in the silicon disk (the white box delineates the disk) generate free-carriers via two-photon absorption (TPA). (c) Schematic depiction of dominant processes in the Si microdisk: TPA, TPA-generated free-carrier density ( $e^-$ ,  $h^+$  denoting electrons and holes, respectively), free-carrier absorption, and surface-state absorption. (d) Schematic of the dispersive effects of heat and free-carriers on the WGM resonance wavelength.

### 3.2. Optical losses

In the previous section, loss rates for the standing wave modes were introduced. These loss rates can be separated into terms reflecting the origin and behavior of each loss mechanism

$$\gamma_{c/s} = \gamma_{c/s,0}^e + \sum_{j>0} \gamma_{c/s,j}^e + \gamma_{c/s,rad} + \gamma_{c/s,lin} + \bar{\gamma}_{c/s,TPA} + \bar{\gamma}_{c/s,FCA}. \quad (3)$$

The total loss rate for each mode includes loss into the forward and backward fiber-taper fundamental modes ( $\gamma_{c/s,0}^e$ ), parasitic losses into other guided modes of the fiber-taper that are not collected ( $\gamma_{c/s,j>0}^e$ ), radiation and scattering losses ( $\gamma_{c/s,rad}$ ), linear material absorption ( $\gamma_{c/s,lin}$ ), two-photon absorption ( $\bar{\gamma}_{c/s,TPA}$ ), and free-carrier absorption ( $\bar{\gamma}_{c/s,FCA}$ ). Note that the coupling coefficient of optical power into the resonator in Eq. (1) is related to  $\gamma_{c/s,0}^e$  by,  $\kappa = \sqrt{\gamma_{c/s,0}^e}/2$ .

In WGM resonators the field distribution can be highly localized, and so the calculation of loss rates due to nonlinear processes must take into account the nonuniform field distribution of a given resonance as well as material properties. We will follow closely the analysis of Barclay [2], with the modification that our analysis will not assume steady-state conditions.

The wavelength region considered in this work ( $\sim 1.5 \mu\text{m}$ ) is within the bandgap of the silicon material of the microdisk resonator, and so linear absorption by the silicon material should be

small. TPA, however, can be significant in silicon [28]. From [2] we have

$$\bar{\gamma}_{c/s,TPA}(t) = \Gamma_{TPA} \frac{\beta_{Si} c^2}{V_{TPA} n_g^2} U_{c/s}(t) \quad (4)$$

where  $c$  is the speed of light in vacuum,  $n_g$  is the group index associated with the measurement of the intensity loss per unit length,  $\beta_{Si}$ , and  $\Gamma_{TPA}$  and  $V_{TPA}$  are defined as [29]

$$\Gamma_{TPA} = \frac{\int_{Si} n^4(\mathbf{r}) |E_{c/s}(\mathbf{r})|^4 d\mathbf{r}}{\int n^4(\mathbf{r}) |E_{c/s}(\mathbf{r})|^4 d\mathbf{r}}, \quad (5)$$

$$V_{TPA} = \frac{\left( \int n^2(\mathbf{r}) |E_{c/s}(\mathbf{r})|^2 d\mathbf{r} \right)^2}{\int n^4(\mathbf{r}) |E_{c/s}(\mathbf{r})|^4 d\mathbf{r}}. \quad (6)$$

The total two-photon absorbed power can then be written as,

$$P_{abs,TPA}(t) = \Gamma_{TPA} \frac{\beta_{Si} c^2}{V_{TPA} n_g^2} \left( U_c^2(t) + U_s^2(t) \right). \quad (7)$$

It should be noted that the above partitioning of nonlinear TPA into separate terms for each of the standing-wave modes is not exactly correct. There are cross-terms due to the non-orthogonality of the modes for processes such as TPA involving higher-order modal overlaps of the electric field distribution [30]. For the standing-wave modes the correction is small, and we neglect the cross-terms in what follows.

The silicon material used in this work has a low doping density ( $N_A < 1 \times 10^{16} \text{ cm}^{-3}$ ). With this doping level, we expect negligible losses due to ionized dopants ( $\alpha_{FCA,0} \sim 10^{-2} \text{ cm}^{-1} \leftrightarrow Q_{FCA,0} \sim 10^7$ ). As such, we will ignore that initial population in our consideration of free-carrier density below. Free-carrier absorption, however, can be significant due to the presence of TPA-generated free-carriers [9, 2, 28]. The optical loss rate due to TPA-induced FCA is given by,

$$\gamma_{c/s,FCA}(\mathbf{r},t) = \frac{\sigma_{Si}(\mathbf{r})c}{n_g} N(\mathbf{r},t), \quad (8)$$

where the absorption cross-section can be estimated from a simple Drude model. This model has been demonstrated to reproduce the behavior of free-carrier absorption for both electron and hole populations in silicon, though with differing absorption cross-sections  $\sigma_{Si}$  for each carrier population [31]. In this expression, the distinction between these populations is ignored and a total cross-section  $\sigma_{Si} = \sigma_{Si,e} + \sigma_{Si,h}$ , and electron-hole pair density  $N(\mathbf{r},t)$  are considered. If we perform the required averaging of this loss rate we find

$$\bar{\gamma}_{c/s,FCA}(t) = \frac{\sigma_{Si} c}{n_g} \overline{N(t)}, \quad (9)$$

where again the  $n_g$  above is the group-index associated with the measurement of the absorption cross-section, and  $\overline{N}$  is defined as

$$\overline{N(t)} = \frac{\int N(\mathbf{r},t) n(\mathbf{r})^2 |E(\mathbf{r})|^2 d\mathbf{r}}{\int n(\mathbf{r})^2 |E(\mathbf{r})|^2 d\mathbf{r}}. \quad (10)$$

Accumulating all these effects, we arrive at a total absorbed power given by,

$$P_{abs}(t) = (\gamma_{c,lin} + \bar{\gamma}_{c,TPA} + \bar{\gamma}_{c,FCA}) U_c(t) + (\gamma_{s,lin} + \bar{\gamma}_{s,TPA} + \bar{\gamma}_{s,FCA}) U_s(t). \quad (11)$$

### 3.3. Dispersion

The nonlinear loss mechanisms discussed above, which change the losses of the WGM resonance in a way dependent on the stored energy, also influence the properties of the resonance. Heating of the resonator due to optical absorption changes its temperature, while the generation of excess free carriers via TPA also changes the refractive index through plasma carrier dispersion [25, 31].

From first order perturbation theory we can estimate the relative change in resonance frequency for a given change in refractive index to be

$$\frac{\Delta\omega_0(t)}{\omega_0} = -\overline{\left(\frac{\Delta n(\mathbf{r},t)}{n(\mathbf{r})}\right)}, \quad (12)$$

where the average of the relative local change in refractive index is [32]

$$\overline{\left(\frac{\Delta n(t)}{n}\right)} = \frac{\int \left(\frac{\Delta n(\mathbf{r},t)}{n(\mathbf{r})}\right) n^2(\mathbf{r}) |E(\mathbf{r})|^2 d\mathbf{r}}{\int n^2(\mathbf{r}) |E(\mathbf{r})|^2 d\mathbf{r}}. \quad (13)$$

Taking into account the effect of heating due to absorption and TPA-induced free-carrier density, and the impact of those effects on the refractive index of the microresonator we have

$$\frac{\Delta n(\mathbf{r},t)}{n(\mathbf{r})} = \frac{1}{n(\mathbf{r})} \frac{dn(\mathbf{r})}{dT} \Delta T(\mathbf{r},t) + \frac{1}{n(\mathbf{r})} \frac{dn(\mathbf{r})}{dN} N(\mathbf{r},t). \quad (14)$$

In Eq. (14)  $\Delta T(\mathbf{r},t)$  is the difference in temperature between the silicon microdisk and its environment. Substituting Eqs. (13) and (14) into Eq. (12) we obtain

$$\frac{\Delta\omega_0(t)}{\omega_0} = -\left(\frac{1}{n_{Si}} \frac{dn_{Si}}{dT} \overline{\Delta T(t)} + \frac{1}{n_{Si}} \frac{dn_{Si}}{dN} \overline{N(t)}\right), \quad (15)$$

where  $\overline{N(t)}$  is defined in Eq. (10) and  $\overline{\Delta T(t)}$  is similarly

$$\overline{\Delta T(t)} = \frac{\int \Delta T(\mathbf{r},t) n^2(\mathbf{r}) |E(\mathbf{r})|^2 d\mathbf{r}}{\int n^2(\mathbf{r}) |E(\mathbf{r})|^2 d\mathbf{r}}. \quad (16)$$

### 3.4. Equations of motion

We can now write down an equation of motion for the temperature of the microdisk resonator through energy conservation considerations [22]. Power is dissipated by optical absorption in the microdisk, adding thermal energy to the silicon microdisk. We assume this process is instantaneous, which is not strictly correct for power dissipated by TPA; TPA can generate phonons on both fast time scales (via intraband relaxation) and on longer time scales (via interband relaxation). This simplifying assumption may contribute to differences between modeled and observed behavior at the shortest time scales. However, for this work, modeling shows the magnitude of FCA heating dominates TPA heating. Thermal energy in the silicon microdisk can escape through radiation, convection, and conduction, processes dependent on position within the microdisk. For the geometry and temperatures considered here convection and radiation can be disregarded, and the microdisk temperature can be assumed to be spatially uniform within the Si layer with little error for the time scales under consideration. We then have, integrating over the disk volume and substituting  $\Delta T(\mathbf{r},t) = \Delta T(t)$  into Eq. (16),

$$\frac{d\overline{\Delta T(t)}}{dt} = -\gamma_{th} \overline{\Delta T(t)} + \frac{\Gamma_{\text{disk}}}{\rho_{Si} c_{p,Si} V_{\text{disk}}} P_{\text{abs}}(t). \quad (17)$$

In the above,  $\Gamma_{\text{disk}}$  represents the fractional energy overlap of the mode with the differential temperature within the Si microdisk,

$$\Gamma_{\text{disk}} = \frac{\int_{\text{Si}} n(\mathbf{r})^2 |E(\mathbf{r})|^2 d\mathbf{r}}{\int n(\mathbf{r})^2 |E(\mathbf{r})|^2 d\mathbf{r}}, \quad (18)$$

and  $\gamma_{th}$  is the silicon microdisk temperature decay rate given by

$$\gamma_{th} = \frac{k}{\rho_{\text{Si}} c_{p,\text{Si}} V_{\text{disk}}}, \quad (19)$$

where  $\rho_{\text{Si}}$ ,  $c_{p,\text{Si}}$ ,  $V_{\text{disk}}$ , and  $k$  are, respectively, the density of silicon, the constant-pressure specific heat capacity of silicon, the volume of the silicon microdisk, and the coefficient of thermal conduction of the  $\text{SiO}_2$  pedestal the microdisk rests upon. For this geometry the coefficient of thermal conduction is approximately  $k = \kappa_{\text{SiO}_2} \pi r_{\text{post}}^2 / h$ , with  $\kappa_{\text{SiO}_2}$  the thermal conductivity,  $r_{\text{post}}$  an average radius, and  $h$  the height of the  $\text{SiO}_2$  pedestal.

We can proceed in a similar fashion to determine the equation of motion for the free-carrier density. A population of free-carriers decays through a variety of processes (non-radiative recombination, diffusion out of the region of interest, Auger recombination, etc). In general, the rate of decay will depend on the position in the microcavity (e.g., due to the proximity of surfaces, impurities) and the density of free-carriers. We will disregard any density dependence in the free-carrier lifetime. The free-carrier population is generated via TPA, and so

$$\frac{\partial N(\mathbf{r}, t)}{\partial t} = -\gamma(\mathbf{r})N(\mathbf{r}, t) + \nabla \cdot (D(\mathbf{r})\nabla N(\mathbf{r}, t)) + G(\mathbf{r}, t). \quad (20)$$

Free-carrier recombination, a process dependent on location (proximity to surfaces, etc.), is represented by the first term on the right hand side (RHS) of Eq. (20), carrier density diffusion is represented by the second, where  $D(\mathbf{r})$  is the electronic diffusion coefficient, and generation is represented by the third term on the RHS. The local generation rate of free-carriers,  $G(\mathbf{r}, t)$  can be calculated by noting that the local TPA photon-loss generates one electron-hole pair per two photons absorbed.

If we then take the mode-average of Eq. (20) we obtain

$$\frac{d\overline{N(t)}}{dt} = -\overline{\gamma(\mathbf{r})N(\mathbf{r}, t)} + \overline{\nabla \cdot (D(\mathbf{r})\nabla N(\mathbf{r}, t))} + \overline{G(t)}. \quad (21)$$

$\overline{G(\mathbf{r}, t)}$  is calculated from the mode-averaged local TPA rate, and as discussed in Ref. [2] can be written as,

$$\overline{G(\mathbf{r}, t)} = \frac{\Gamma_{\text{FCA}} \beta_{\text{Si}} c^2}{2\hbar \omega_p n_g^2 V_{\text{FCA}}^2} (U_c(t)^2 + U_s(t)^2), \quad (22)$$

where  $\Gamma_{\text{FCA}}$  and  $V_{\text{FCA}}$  are given by,

$$\Gamma_{\text{FCA}} = \frac{\int_{\text{Si}} n^6(\mathbf{r}) |E_{c/s}(\mathbf{r})|^6 d\mathbf{r}}{\int n^6(\mathbf{r}) |E_{c/s}(\mathbf{r})|^6 d\mathbf{r}}, \quad (23)$$

$$V_{\text{FCA}}^2 = \frac{\left( \int n^2(\mathbf{r}) |E_{c/s}(\mathbf{r})|^2 d\mathbf{r} \right)^3}{\int n^6(\mathbf{r}) |E_{c/s}(\mathbf{r})|^6 d\mathbf{r}}. \quad (24)$$

As in the case of TPA, we neglect in the FCA higher-order field overlaps between the cosine- and sine-like standing-wave modes, a small approximation in this case.

For free-carrier lifetimes  $\gtrsim 1$  ns, extensive free-carrier diffusion and the high localization of the field distribution of the resonant mode result in an effectively constant free-carrier density over the regions where there is appreciable optical energy density. We may then approximate the free-carrier density to be constant for purposes of mode-averaging, and the second term in the RHS of Eq. (21) can be neglected. The first term in the RHS of Eq. (21) becomes an effective free-carrier decay rate of the mode-averaged free-carrier density, accounting for both recombination and diffusion, and we finally have

$$\frac{d\overline{N}(t)}{dt} = -\gamma_{fc}\overline{N}(t) + \frac{\Gamma_{FCA}\beta_{Si}c^2}{2\hbar\omega_p n_g^2 V_{FCA}^2} (U_c(t)^2 + U_s(t)^2). \quad (25)$$

Equation (25) is an equation of motion for the mode-averaged free-carrier density, where  $\omega_l$  is the frequency of the laser coupled into the WGM from the fiber-taper.

#### 4. Comparison between experiment and theory

Equations (1-3),(15),(17), and (25) comprise a model that we can numerically integrate, allowing us to determine the dynamical behavior of the system. The numerical integration is carried out using a predictor-corrector method [33]. In this model, the free-carrier and the thermal decay rate are taken as free parameters. The fixed parameters of the model are measured values, where possible (input power, resonance  $Q$ s and coupling values, geometry of the disk, etc.), values taken from the literature ( $\beta_{Si}$ ,  $\sigma_{Si}$ , etc.), and values calculated via the finite-element-method for quantities not amenable to measurement (mode-field profiles, overlap factors, mode volumes, etc.). These parameters are presented in Table 1.

Figure 5(a) compares the results of simulation and experiment for an input laser power corresponding to the experimental conditions of Fig. 2(b) and a laser wavelength near the onset of oscillation (red oval) in Fig. 2(b)). The transmitted optical power of the simulation is shown to accurately estimate both the observed transmission dip, temporal width, and the period of repetition. The salient trends in the period and duty cycle of the transmission oscillations observed experimentally (Fig. 3) are also recovered by the model. The inset of Fig. 5(a) shows a zoomed-in comparison of the transmission dip. The model is also seen to accurately predict the initial rapid double-dip, slow increase in the transmission depth, and the more elongated double-dip just before transmission recovery. As discussed below, we can now relate these features to the rapid shifting of the two standing-wave WGM resonances back-and-forth through the pump laser.

In Fig. 5(b-c) we show the corresponding simulated temporal behavior of the internal optical cavity energy, Si microdisk temperature, free-carrier population, free-carrier dispersion, and thermal dispersion. From these model parameters a clearer picture is revealed of how the oscillations of the transmitted optical power occur, and what the identifiable features of the transmission oscillations correspond to. We have isolated four distinct regions labelled (i)-(iv) in Fig. 5: (i) with the microdisk standing-wave WGM resonances initially slightly red detuned of the pump laser there occurs a transient rapid generation of free-carriers due to TPA which causes the WGMs to rapidly blue shift past the pump laser wavelength, (ii) the heat generation from FCA eventually stops the rapid blue-shift and there begins a slow red-shift of the WGM resonances towards the laser pump and a large build-up of free-carriers and thermal energy within microdisk, (iii) eventually the WGM resonances red-shift into and through the laser pump at which time there is a rapid reduction in the internal optical energy and free-carrier population (both of which decay much faster than the thermal energy), and this results finally in (iv) a large residual red-shift of the WGM resonances and thermal energy (phonon population) within the microdisk that slowly decays through the SiO<sub>2</sub> pedestal and into the Si substrate.

Table 1. Parameters used in the Si microdisk model.

Parameter	Value	Units	Source
$n_{\text{Si}}$	3.485	-	[34]
$dn_{\text{Si}}/dT$	$1.86 \times 10^{-4}$	$\text{K}^{-1}$	[25]
$dn_{\text{Si}}/dN$	$-1.73 \times 10^{-27}$	$\text{m}^3$	[31]
$\beta_{\text{Si}}$	$8.4 \times 10^{-12}$	$\text{m} \cdot \text{W}^{-1}$	[35]
$\sigma_{\text{Si}}$	$1 \times 10^{-21}$	$\text{m}^2$	[36]
$V_{\text{TPA}}$	46	$(\lambda_0/n_{\text{Si}})^3$	FEM
$V_{\text{FCA}}$	39.9	$(\lambda_0/n_{\text{Si}})^3$	FEM
$\Gamma_{\text{TPA}}$	0.99	-	FEM
$\Gamma_{\text{FCA}}$	0.99	-	FEM
$\rho_{\text{Si}}$	2.33	$\text{g} \cdot \text{cm}^{-3}$	[37]
$c_{p,\text{Si}}$	0.7	$\text{J} \cdot \text{g}^{-1} \cdot \text{K}^{-1}$	[37]
$\Gamma_{\text{disk}}$	0.99	-	FEM
$\gamma_{c,o}$	4.1	GHz	low-power meas.
$\gamma_{s,o}$	5.8	GHz	low-power meas.
$\gamma_{c/s,\text{lin}}$	0.86	GHz	low-power meas.
$\gamma_{\beta}$	14.3	GHz	low-power meas.
$\kappa$	1.5	$\text{GHz}^{1/2}$	low-power meas.
$\lambda_o$	1453.98	nm	low-power meas.
$ s ^2$	480	$\mu\text{W}$	measured
$\lambda_{l,\text{exp.}}$	1454.36	nm	measured
$\lambda_{l,\text{model}}$	1454.12	nm	model
$\gamma'_{\text{fc}}$	98	MHz	fit
$\gamma_{th}$	0.15	MHz	fit

After the microdisk has cooled and the WGM resonances are only slightly red-detuned from pump laser, the cycle repeats.

From the above description it is apparent that the oscillations are initiated by a transient blue-shift of the microdisk WGM resonances due to free-carriers. Equations (25), (17), and (15) show that the rapid generation rate of free-carriers due to TPA results in a proportional rapid rate of WGM blue-shift, whereas the rate of WGM red-shift due to FCA heating is only proportional to  $\overline{N(t)}$  (not  $\dot{\overline{N(t)}}$ ) and is thus delayed relative to the FCD blue-shift. If the mode volume of the microresonator is small enough, the input optical power large enough, and the optical resonance linewidth narrow enough, then the transient FCD blue-shift can be large enough to sweep the optical resonance through the pump laser wavelength. For geometries and materials in which the thermal resistance of the microresonator is large, then this initial blue-shift will be transient and the thermal red-shift of the optical resonance will eventually dominate, resulting in oscillations of the sort observed in the Si microdisk structures studied here.

Numerical experiments indicate that the system trajectory is a stable limit-cycle; for a given input wavelength displaying the self-induced oscillations, significant perturbations of the temperature or free-carrier density from the stable trajectory decay back to the stable trajectory, a

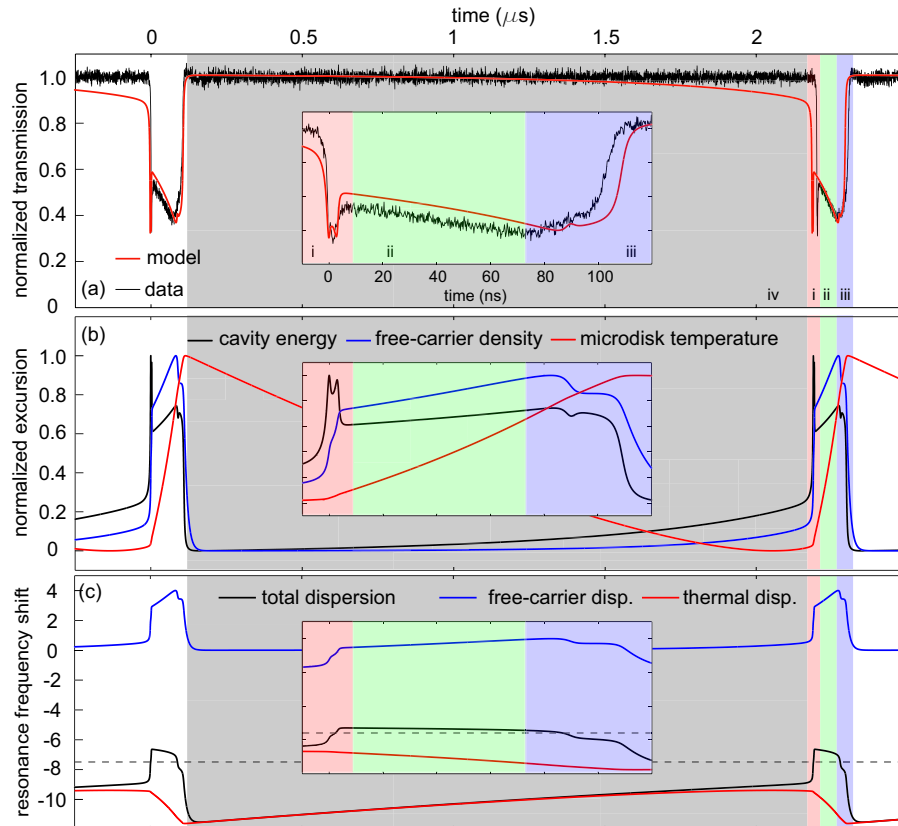


Fig. 5. Comparison between model and measurement. The shaded regions (i), (ii), (iii), and (iv) correspond to different phases of the dynamics as described in the text. (a) Comparison of the modeled and measured time-dependent normalized optical transmission. (b) Normalized excursion of the modeled optical cavity energy, free-carrier density, and differential microdisk temperature. The normalization for a function  $f(t)$  is calculated as  $\frac{f(t) - \min(f(t))}{\text{range}(f(t))}$ . The differential temperature covers the range  $\Delta T = 1.9 - 2.4$  K, the free-carrier density covers the range  $N = 1 \times 10^{14} - 0.9 \times 10^{17} \text{ cm}^{-3}$ , and the stored optical cavity energy ranges from  $U = 0.8 - 29$  fJ (c) Resonance frequency shift (in units of  $\gamma_\beta$ ), broken into thermal and free-carrier contributions. The dashed line indicates the pump laser wavelength ( $\lambda_l$ ). The insets within each of (a), (b), and (c) corresponds to a narrow time-slice about the transmission dip.

characteristic of a limit cycle [38]. Neither the experimental measurements nor the numerical model showed hysteresis in the threshold pump laser wavelength for the onset of oscillations, which is indicative of a super-critical as opposed to sub-critical Hopf-bifurcation [38, 39]. In the language of nonlinear systems theory, as the pump laser wavelength is tuned into resonance from the blue-side of the microdisk WGMs, a super-critical Hopf-bifurcation results and a stable limit cycle ensues.

## 5. Summary and conclusions

In this work we have presented observations of thermo-optical bistability in a high- $Q$  SOI microdisk resonator with input powers as low as  $35\ \mu\text{W}$ . For slightly higher input powers of  $60\ \mu\text{W}$  self-induced oscillations in the transmitted optical power of  $\mu\text{s}$  period and  $\sim 100\ \text{ns}$  pulse-width are observed. A time-domain model relating the temperature of the microdisk, the free-carrier density in the microdisk, the optical energy stored in the microdisk, and the WGM resonance wavelength was developed and applied to explain the observations. Good agreement was found between the proposed model and observation. An effective free-carrier lifetime of  $10\ \text{ns}$  is inferred from the model, a value consistent with those reported in similar SOI microphotonic structures [2, 28].

Significant interest in using Si microresonators for optical modulation [40, 41], all-optical switching [2, 3, 4, 5, 42], and optical memory elements [6] suggests that microphotonic resonators will find many applications in future devices. The work presented here, however, illustrates that high- $Q$  microphotonic resonators can be very strongly impacted by optically-induced variations in temperature and carrier density. While there may be novel applications for the self-oscillation phenomenon presented here, it is most important as an example of the possible ramifications of using scaled, high- $Q$  devices: decreased optical thresholds for nonlinear processes and the rapid time scales involved may become critically important to device performance. These nonlinearities and their interactions may in some cases necessitate the implementation of dynamic control of the nonlinear system, for example by the active control of carriers in the optical device [5, 43, 44]. Such effects will only become more critical in yet smaller, higher quality devices, such as the recently demonstrated Si photonic crystal resonators with  $Q \sim 1 \times 10^6$  and  $V_{\text{eff}} \sim 1.5 (\lambda/n)^3$  [45].